Exploring Structural Anisotropy in Amorphous Tb-Co via Changes in Medium-Range Ordering

Ellis Kennedy, Emily Hollingworth, Alejandro Ceballos, Daisy O'Mahoney, Colin Ophus, Frances Hellman, Mary Scott

Microscopy and Microanalysis, 2025, **31**, ozae113
https://doi.org/10.1093/mam/ozae113
Advance access publication 14 November 2024
Original Article

Microscopy AND Microanalysis

Exploring Structural Anisotropy in Amorphous Tb-Co via Changes in Medium-Range Ordering

Ellis Kennedy[1], Emily Hollingworth[2,3], Alejandro Ceballos[1,3], Daisy O'Mahoney[1], Colin Ophus[4], Frances Hellman[1,2,3], and Mary Scott[1,4,*]

[1]*Department of Materials Science and Engineering, University of California Berkeley, Berkeley, CA 94720, USA*
[2]*Department of Physics, University of California Berkeley, Berkeley, CA 94720, USA*
[3]*Materials Science Division, Lawrence Berkeley National Laboratory, Berkeley, CA 94720, USA*
[4]*NCEM, Molecular Foundry, Lawrence Berkeley National Laboratory, Berkeley, CA 94720, USA*

***Corresponding author:** M. Scott, E-mail: mary.scott@berkeley.edu

Abstract

Amorphous thin films grown by magnetron co-sputtering exhibit changes in atomic structure with varying growth and annealing temperatures. Structural variations influence the bulk properties of the films. Scanning nanodiffraction performed in a transmission electron microscope (TEM) is applied to amorphous $Tb_{17}Co_{83}$ (*a*-Tb-Co) films deposited over a range of temperatures to measure relative changes in medium-range ordering (MRO). These measurements reveal an increase in MRO with higher growth temperatures and a decrease in MRO with higher annealing temperatures. The trend in MRO indicates a relationship between the growth conditions and local atomic ordering. By tilting select films, the TEM measures variations in the local atomic structure as a function of orientation within the films. The findings support claims that preferential ordering along the growth direction results from temperature-mediated adatom configurations during deposition, and that oriented MRO correlates with increased structural anisotropy, explaining the strong growth-induced perpendicular magnetic anisotropy found in rare earth–transition metal films. Beyond magnetic films, we propose the tilted FEM workflow as a method of extracting anisotropic structural information in a variety of amorphous materials with directionally dependent bulk properties, such as films with inherent bonding asymmetry grown by physical vapor deposition.

Key words: amorphous materials, magnetic materials, medium-range order, 4D-STEM

Introduction

Structural studies of amorphous materials are challenging due to an inability to apply fundamental characterization techniques relying on long-range ordering and crystallographic symmetries (Bernal & Mason, 1960; Voyles & Muller, 2002). Nonetheless, amorphous materials are ubiquitous and used for a variety of applications, including as bulk metallic glasses and amorphous oxides where it is well known that growth parameters are directly correlated with properties. Metallic glasses are one of the most studied types of metals because of their achievable strength and toughness properties (Greer, 1995; Cheng & Ma, 2011). Amorphous oxides have a range of uses, including as protective coatings (Kiryukhantsev-Korneev et al., 2022) and for energy storage (Yu et al., 2023). Recently, scientific advances have broadened the scope of applications of amorphous materials, including in battery technologies (Ding et al., 2024; Zhu et al., 2024), optoelectronic devices (Lim et al., 2019; Ganguly, 2023), and magnetic materials (Cirillo et al., 2020).

An example of an amorphous magnetic system, amorphous rare earth–transition metal (RE–TM) alloys have tunable magnetic properties, such as magnetization (M), compensation temperature, magnetic coercivity (H_c), and perpendicular magnetic anisotropy (PMA, parameterized through the uniaxial anisotropy constant K_{ui}) (Hasegawa et al., 1974; Hellman & Gyorgy, 1992; Harris et al., 1993, 1994; Andreenko & Nikitin, 1997; Gambino, 1998; Ding & Poon, 2013). These properties make them desirable as novel spintronic materials and for ultrafast magneto-optical recording devices. Out-of-plane (OOP) RE–TM bonding and in-plane (IP) TM–TM bonding have been correlated to magnetization and bulk PMA in *a*-RE–TM systems (Hellman & Gyorgy, 1992; Harris et al., 1993, 1994). The amorphous nature of these systems complicates their analysis, as variations in bulk magnetic properties may arise from subtle variations in local atomic ordering (Cochrane et al., 1978). Previous work shows that many magnetic properties, including PMA and M, are independent of film thickness, surface layer magnetic interactions, and macroscopic growth-induced strain (Hellman & Gyorgy, 1992). The present work analyzes sputtered amorphous $Tb_{17}Co_{83}$ and focuses on the relationship between magnetic properties, particularly H_c and PMA, and atomic ordering; the approach presented here to study microstructural anisotropy can be applied more generally to a wide range of amorphous films.

The succinct description of crystalline structures with defined unit cells and permitted symmetry operations does not extend to amorphous materials. Their lack of translational and rotational symmetry requires a statistical approach for analysis (Voyles & Muller, 2002; Treacy et al., 2005). Two-body and multi-body distribution functions are applied to the study of amorphous structures to determine the

Received: June 12, 2024. **Revised:** October 1, 2024. **Accepted:** October 23, 2024

probability that two or more atoms will be separated by a specific distance. Short-range ordering (SRO) is probed through two-body statistical analysis, such as radial distribution functions. However, SRO is limited to the first few shells of the constituent atom. Looking out a little further, medium-range ordering (MRO) on the 0.5–5 nm length scale, can be probed with transmission electron microscopy (TEM) by using fluctuation electron microscopy (FEM) (Williamson, 1995; Voyles & Muller, 2002). Statistical analysis of MRO can determine the degree and type of ordering that exists between the extremes of long-range and short-range order (Nakhmanson et al., 2001; Treacy et al., 2005).

In this work, *a*-$Tb_{17}Co_{83}$ is used as a representative ferrimagnetic *a*-RE–TM system, and, even more broadly, as a representative amorphous film that was grown *via* sputtering. TEM analysis of these materials is conducted to probe relationships between atomic configuration and growth conditions. A series of *a*-$Tb_{17}Co_{83}$ films were deposited at 20, 200, and 300°C. The films then either received no further heat treatment or were annealed at 200 or 300°C. For films of this type, previous studies indicate that the PMA and coercivity were found to increase with growth temperature and decrease with annealing temperature (Hasegawa et al., 1974; Hellman & Gyorgy, 1992; Mergel et al., 1993; Ceballos et al., 2021). The TEM method of scanning nanodiffraction was used to probe the underlying structural mechanisms responsible for variations in the magnetic properties of *a*-$Tb_{17}Co_{83}$ as a function of film deposition and annealing temperature. The relative MRO across the series of samples is measured with FEM, a specialized application of scanning nanodiffraction that is sensitive to changes in diffracted intensity related to variations in atomic configurations within an amorphous system (Voyles & Muller, 2002). We determine that MRO in the films increases with higher deposition temperatures and decreases with higher annealing temperatures. The results support the model of magnetism in *a*-RE–TM systems in which OOP magnetization is related to atom-specific preferential local atomic ordering. The analysis provides a pathway for research correlating growth-induced structural anisotropy to measured material properties in amorphous systems.

Experimental Details

a-$Tb_{17}Co_{83}$ films were produced using magnetron co-sputtering at 1.8 mTorr Ar pressure from separate Tb and Co targets. The base pressure of the chamber was 7×10^{-8} Torr. The *a*-$Tb_{17}Co_{83}$ films were sputtered at room temperature (20°C), 200, and 300°C with a capping layer of *a*-SiN_x sputtered at 3.0 mTorr of Ar pressure. The films were deposited on Norcada grids with 10 nm thick *a*-SiN_x membranes. Samples consisted of 30 nm *a*-$Tb_{17}Co_{83}$ films capped with 10 nm of *a*-SiN_x to prevent oxidation. The 30 nm thickness was selected for the *a*-$Tb_{17}Co_{83}$, as it was experimentally determined to produce a strong speckle intensity in scanning nanodiffraction. A control sample of 10 nm of *a*-SiN_x was sputtered at 3.0 mTorr of Ar pressure to determine the influence of the capping layer on the diffraction data. After deposition at 20°C, some films were annealed at 200 or 300°C for an hour under high vacuum.

The magnetization as a function of applied magnetic field OOP was measured in a Quantum Design Magnetic Properties Measurement System (MPMS) at 20°C for a series of samples grown and annealed under identical conditions to those detailed above (Supplementary Fig. S1 of supplementary materials). The films grown at 20°C were annealed for an hour at 150, 200, 275, and 350°C to establish how OOP magnetization and H_c depend on annealing temperature. The applied field was varied between −1 and 1 T, a range exceeding the magnetic saturation values for all samples. The PMA was derived in Ceballos-Sanchez (2019) for these same films, and shows that the PMA increases with deposition temperature and decreases with annealing temperature as has been seen in other work on *a*-RE–TM alloys. For all samples, $T_c = 190$°C (Supplementary Fig. S2 of the supplementary materials), $T_{comp} = -73$°C, and M_s is 150 emu/cc. These measurements depend strongly on composition, so their consistency shows that no significant compositional variations have occurred with changing growth temperature or upon annealing.

A subset of the films measured with magnetometry were analyzed using FEM. To measure changes in the MRO of the films, FEM experiments were carried out using scanning transmission electron microscopy (STEM) in an FEI TitanX operated at an accelerating voltage of 200 kV and a 2.2 nm diameter probe. The third condenser lens was set to produce a convergence angle of 0.51 mrad resulting in a measured 2.2 nm diameter probe and a 15.5 pA probe current. Images were collected on an Orius charge-coupled device (CCD) detector with an exposure time of 0.3 s and a camera length of 300 mm. The images were binned by a factor of four, to a final size of 512 × 512 pixels. Scanning nanodiffraction data were collected as 12 × 12 image stacks (144 images per stack) for each film with 5 nm step sizes between regions of analysis. Collection was repeated five times per film for statistical averaging over different regions of the film and to avoid excess contamination. During the experiment, all diffraction patterns were taken with the same imaging conditions to ensure that the effects of microscope misalignment were the same across all patterns. The small features that appears around 6 and 7.1 nm^{-1} in all variance curves is from a defect on the CCD, as can be observed in the data available at https://zenodo.org/records/8045363.

Additionally, the films deposited at 20 and 300°C were tilted at an angle varied between 0 and 40° in 5° increments to determine whether MRO varies with orientation through the film. These two films were selected for tilting because they had the greatest difference in MRO as determined from FEM variance measurements. For the tilted data sets, collection was repeated five to seven times. No additional preparation of the sputtered SiN_x-capped *a*-$Tb_{17}Co_{83}$ films was required for FEM analysis. The analysis was performed following the method outlined by Kennedy et al. (2020). The procedures for collecting scanning nanodiffraction data and FEM analysis are further detailed in Figure 1 and in the Supplementary Materials. Error bars were computed from the standard deviation of *V(k)* values as a function of the scattering vector.

For FEM, the variance is calculated with respect to scattering angle **k**, position on the sample *r*, and resolution (which is a function of *r*); however, in STEM FEM only the scattering vector varies and thus the equation for variance V_σ in diffracted intensity $I(\mathbf{k})$ becomes (Treacy et al., 2005):

$$V_\sigma(\mathbf{k}, r) = \frac{\langle I^2(\mathbf{k}, r)\rangle - \langle I(\mathbf{k}, r)\rangle^2}{\langle I(\mathbf{k}, r)\rangle^2}, \quad (1)$$

Additionally, Lorentz TEM images were collected from the as-deposited film grown at 20°C and the film grown at 20°C and

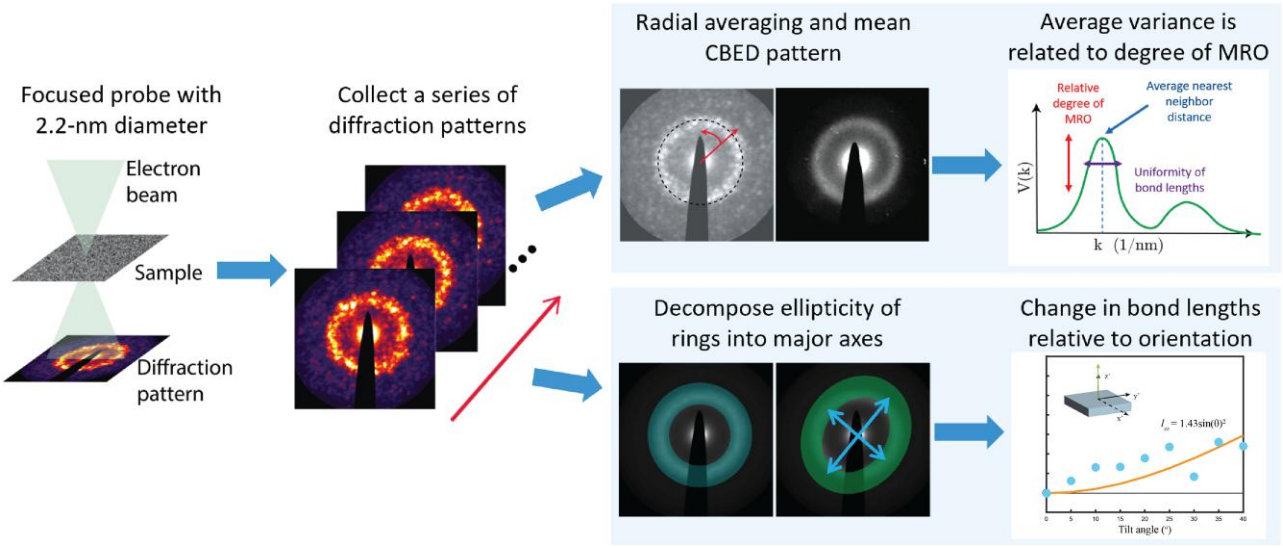

Fig. 1. Representative workflow for collecting scanning nanodiffraction data and FEM analysis of variance in speckled intensity. The electron beam is focused to a probe in STEM mode and the sample is placed at eucentric height to produce the characteristic speckled pattern of FEM. The beam is rastered across multiple regions of the film to collected a series of scanning nanodiffraction patterns.

annealed at 200 and 300°C to probe the effect of annealing on magnetic domain structure and to confirm the magnetic coercivity measurements from the annealed films. All films had been previously subjected to a magnetic field of ≈2 T during FEM image acquisition, but the magnetic field of the objective lens was minimized to <0.1 T for Lorentz imaging. The films were tilted 15° and the beam was defocused to produce visible magnetic domains. A larger defocus was required to view the domain structure in the film annealed at 300°C compared to the two other films depicted.

Results

The magnetic coercivity H_c is 183 mT for films grown at 20°C, and increases for films grown at 200 and 300°C. For films grown at 20°C and subsequently annealed at temperatures between 150 and 350°C, H_c decreases with temperature. The relationships between deposition temperature, annealing temperature, and H_c are shown in Supplementary Figure S1 of the supplementary materials and are consistent with the results in Ceballos-Sanchez (2019) and Ceballos et al. (2021). Similar trends have been shown in other amorphous RE–TM thin film systems (Hellman & Gyorgy, 1992; Harris et al., 1994). Importantly, the OOP magnetic saturation M_s remains constant (150 emu/cc) for all samples in the series as does the compensation temperature.

High-resolution TEM imaging and the mean converged beam electron diffraction (CBED) patterns confirm that all samples are amorphous (shown in Supplementary Fig. S3 of the supplementary materials). The uniformity of the diffracted speckle in the scanning nanodiffraction patterns and lack of strong Bragg scattering indicates that the films lack long-range order and contain no nanocrystals.

In Figure 2, the normalized variance in intensity $V(\boldsymbol{k})$ for films in their as-deposited state (a) and after annealing (b) is plotted as a function of scattering vector using mean statistics. The MRO increases with increasing growth temperature, as indicated by an increase in $V(\boldsymbol{k})$. The variance for the 300°C growth is significantly sharper than the 20 and 200°C variances. There is an increase in the $V(\boldsymbol{k})$ and a decrease in the full width at half maximum (FWHM) across the three films as a function of deposition temperature. Additionally, the film grown at 300°C exhibits a shoulder feature between 3.5 and 4.0 nm^{-1}, indicative of a second preferential bonding configuration in addition to the primary MRO distance at 4.8 nm^{-1}. As the shoulder is only visible in the high-temperature growth, it is likely a result of higher adatom energy during deposition. Notably, the small features that appears around 6 and 7.1 nm^{-1} in all variance curves is from a defect on the CCD, as can be observed in the data available at https://zenodo.org/records/8045363.

The peak heights correspond to relative MRO and the peak positions correspond to the mean interatomic distance of the MRO. The peaks in $V(\mathbf{k})$ are typically attributable to oriented clusters of atoms (MRO) and not to individual bond types (SRO) (Voyles & Muller, 2002; Li et al., 2014). Two main peak features emerge in the variance plots in Figure 2. The first peak is centered between 2 and 3 nm^{-1} and is attributable to a-SiN_x, as confirmed through FEM analysis of 10 nm of a-SiN_x deposited onto a-SiN_x membranes. The most prominent peak is centered between 4.5 and 4.8 nm^{-1} and originates from the a-$Tb_{17}Co_{83}$. The peak positions of the a-$Tb_{17}Co_{83}$ growth series shift to larger $\boldsymbol{k}$ values with increasing deposition temperature. The change in the magnitude of the a-$Tb_{17}Co_{83}$ peak variance relates to degree of MRO in the films. The scattering vector $\boldsymbol{k}$ associated with each peak is a measure of atom clusters oriented close to a diffraction angle and does not directly relate to specific bond lengths (Voyles & Muller, 2002). Peak positions and relative heights are provided in Table 1. The peaks were fit as single Gaussians using the top 10% of the variance curves for an estimate of the maximum peaks' height, scattering energy, and FWHM.

The FEM diffracted signal varies slightly as a function of orientation through the individual films, as shown in Figure 3, suggesting directional dependency in bonding structure. The most significant difference in MRO as a function of tilt angle was observed between the films grown at 20 and 300°C. These films were tilted in the TEM to 40°C to check

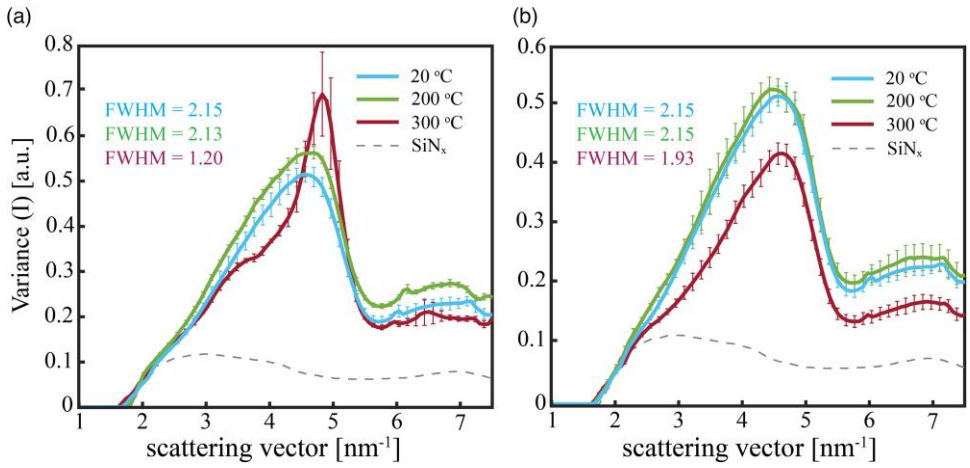

Fig. 2. Variance as a function of scattering vector **k** for *a*-$Tb_{17}Co_{83}$ films (**a**) deposited at 20, 200, and 300°C and (**b**) subsequently annealed at 200 and 300°C following deposition at 20°C. The height of the peak centered between 4.5 and 4.8 nm^{-1} corresponds to the degree of relative MRO in the films. The magnitude of the peak increases with growth temperature, indicating that MRO is greater for films deposited at higher temperatures. The position of the peaks along the scattering vector axis indicates the average size of the bonds resulting in detectable MRO. The dashed gray lines are the variance in intensity of the SiN_x control film.

Table 1. Summarized Relative Peak Heights and Positions along the Scattering Vector ***k*** Axis from FEM Curves in Figure 2.

Temperature Parameters	Height[a]	Position (nm^{-1})
20°C deposition	1	4.5
200°C deposition	1.10	4.5–4.7
300°C deposition	1.23	4.8
20°C deposition, 200°C anneal	1.01	4.5
20°C deposition, 300°C anneal	0.81	4.6

[a]The peak height of the film grown at 20°C is used as the reference. Other peak heights are given relative to it.

for directional dependency of the MRO. Changes in the ellipticity of the FEM patterns as a function of tilt angle reveal that the films deposited at 300°C exhibit a greater change in the length of their major axes, compared to the major axes of the films grown at 20°C. The mean bond length of both films decreases as a function of orientation away from the film normals. The decrease is more pronounced for the film deposited at 300°C, indicating greater orientation-dependency of the MRO bond lengths. By assigning the changes in the FEM diffraction rings to changes in bond length in the IP and OOP directions, we can analyze the tilted data using strain relationships (Supplementary Fig. S4 of the supplementary materials). From this, we determine that the maximum change in mean bond length is 1.43% for the film deposited at 20°C and 3.14% for the film deposited at 300°C. These values assume the trend continues past the 40°C tilt angle, to the OOP orientation. This implies that the films grown at 300°C have greater directional dependence of interatomic ordering.

Discussion

Many models have been proposed for the origin of PMA and changing coercivity in amorphous RE–TM thin films. Proposals include columnar microstructures, anelastic strains, surface layer-induced anisotropy, growth-induced anisotropy resulting from magnetic interactions, and temperature-mediated subtle alignments of atoms around the RE atoms (Clark, 1973; Leamy & Dirks, 1978; Dirks & Gijsbers, 1979; Yan et al., 1991; Fu & Mansuripur, 1992; Hellman & Gyorgy, 1992). The mechanism described in the latter of these models is commonly referred to as amorphous phase texturing (Hellman & Gyorgy, 1992). Many of these models have been disproven by varying growth parameters and measuring the resulting variations in magnetization. This work supports the model of texturing in which local adatom configurations arrange themselves to minimize surface energy during the deposition process.

In *a*-$Tb_{17}Co_{83}$, the itinerant *3d*-electrons of Co influence the magnetic ordering of the localized *4f*-electrons of Tb (RE) through an antiferromagnetic exchange interaction (Brooks et al., 1989). The magnetic moments of the Tb *4f*-electron orbitals, which are more than half-filled, align antiferromagnetically to the moments of the Co (TM) atoms. The combined effect of the resulting negative exchange together with local uniaxial anisotropy, which acts primarily on the Tb moments, is to produce noncolinear ferrimagnetism that is Co-dominant above T_{comp} and Tb-dominant below T_{comp} (Vas'kovskiy et al., 2015; Finley & Liu, 2016). *a*-$Tb_{17}Co_{83}$ has a T_{comp} of approximately −83°C, making it Co-dominant at 20°C. The Curie temperature (T_C) of *a*-$Tb_{17}Co_{83}$ is ≈190°C. The coercivity and PMA increase with increasing growth temperature in the *a*-$Tb_{17}Co_{83}$ system (shown in Supplementary Fig. S1), including for films grown above T_C (Ceballos-Sanchez, 2019; Ceballos et al., 2021). The same trend has been independently observed in other amorphous RE–TM systems (Kobayashi et al., 1983; Hellman et al., 1989; Hajjar et al., 1990; Hellman & Gyorgy, 1992; Andreenko & Nikitin, 1997; Zhang et al., 2010).

The glass transition temperature (T_g) for Tb-Co alloys is unreported in literature. A comparable system, Gd-Co alloys, exhibit T_g values between 307 and 327°C (Xue et al., 2022), while Fe-Tb displays an amorphous to crystalline transition within the range of 400 to 600°C for similar Tb at.% compositions (Hellman et al., 1989). Assuming T_g is most influenced by the TM atoms, we estimate a T_g between 307 and 327°C, not much higher than the 300°C used for annealing and growth of some films. Ultra-stable glasses are typically found for films grown near 0.8–0.85 T_g, or 200–230°C for our

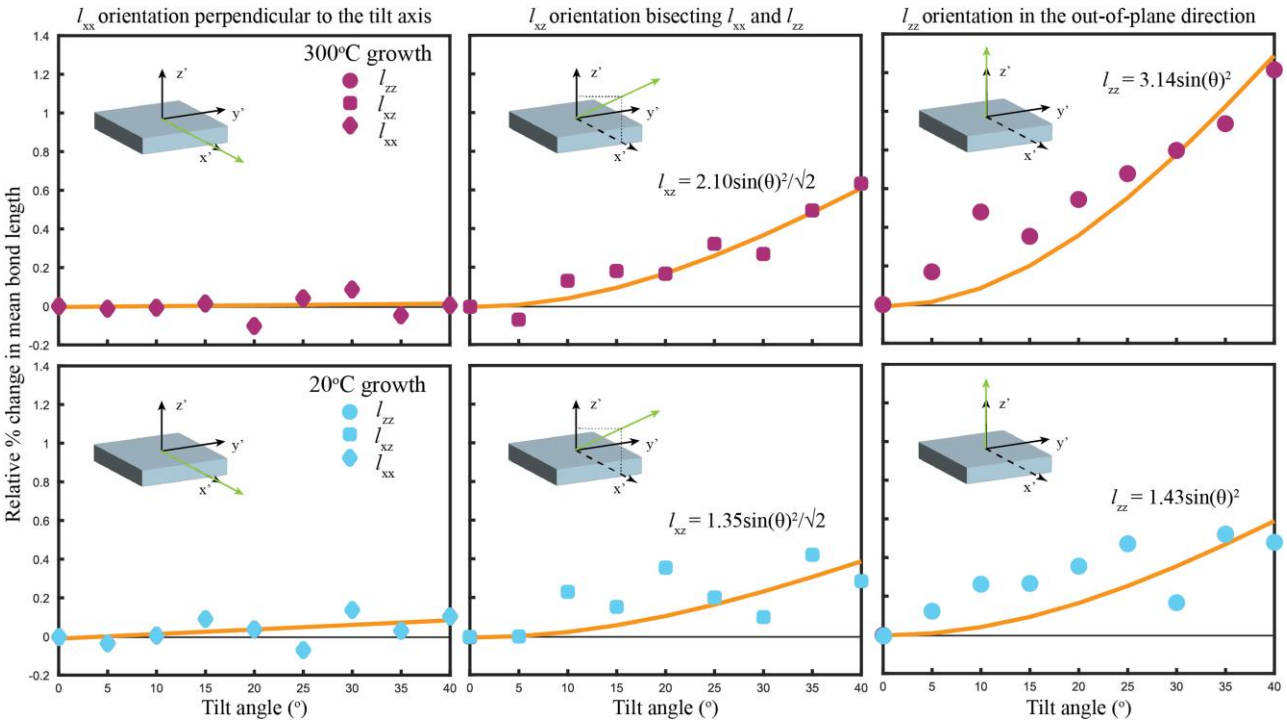

Fig. 3. Relative % change in mean bond distances as a function of tilt angle for the films deposited at 20 and 300°C. The 20°C data are shown in the bottom row with blue data markers and the 300°C data are shown in the top row with magenta markers. The 0° mean bond length is set to zero for all orientations. The *z*′-oriented strain changes with tilt angle as the orientation changes from IP (0° tilt) to OOP (extrapolated to 90° tilt). The film deposited at 300°C exhibits a greater degree of change in relative bond lengths compared to the film deposited at 20°C. The measured % changes in mean bond length are modeled by the infinitesimal strain theory applied to a rotated system, as shown by the plotted curves. The green arrows in the insets show the orientation of each *l* component at 90° (experimentally inaccessible).

estimated T_g (Sun et al., 2016). The 200°C film was thus deposited close to the estimated ultra-stable glass temperature, while the 20°C growth is well below, and 300°C growth well above, both likely leading to lower stability glasses than for films grown at 200°C. Annealing at temperatures below crystallization but as close as possible to T_g leads to increased stability, consistent with the FEM data in this paper.

There is an inverse trend between the H_c and PMA and annealing temperature. Similarly, as the annealing temperature increases, the MRO decreases, as shown in Figure 2 and summarized in Table 1. Thus, increased deposition temperature increases MRO and magnetic anisotropy and coercivity, while increased annealing temperature reduces MRO, magnetic anisotropy, and coercivity in *a*-$Tb_{17}Co_{83}$. The $\boldsymbol{V}(\boldsymbol{k})$ curves for the 20°C growth and the film annealed at 200°C are similar with nearly identical FWHM, position, and relative height. The similarity suggests that there is a minimum temperature required for MRO atomic rearrangement during annealing. With an estimated T_g just above 200°C, it is likely that an anneal temperature close to the T_g is required for rearrangement into an ultra-stable glass. Overcoming the energy barrier for atomic re-orientation detectable with FEM requires a long enough anneal time and high enough temperature. At 300°C for one hour, the annealing parameters are sufficient to allow energy-minimizing atomic rearrangement in the bulk of the film.

Above T_C, the system is paramagnetic and atomic interactions are not governed by magnetic interactions. Thus, the trend in MRO for the *a*-$Tb_{17}Co_{83}$ growth series cannot be ascribed to magnetic interactions. Instead, the relationship between MRO and growth temperature-mediated magnetic anisotropy supports models in which local adatom configurations arrange such that they minimize the surface energy during growth (Hellman, 1994). As layers build, the preferential configuration is preserved, leading to oriented local magnetic anisotropy that produces an overall macroscopic change in bulk magnetization of the system.

The films grown at 20 and 300°C were selected for tilted FEM analysis to understand the relationship between temperature-mediated atomic texturing during deposition and orientationally anisotropic MRO (Kennedy et al., 2020). In this measurement, FEM data is acquired at varying stage tilt angles, which enables us to deduce the relative change in bond lengths associated with the MRO in the IP and OOP directions. Because the diffraction patterns contain information about d-spacings perpendicular to the direction of the beam, as the effective angle between the beam and the sample is varied, any changes in bond length between the IP and OOP directions in the film will cause an ellipticity in diffraction pattern (Supplementary Materials). Since the beam samples bond lengths in the directions perpendicular to the propagation direction, changing the sample tilt angle samples different directions in the film. Specifically, tilting the sample probes bond lengths that lie OOP in the direction perpendicular to the tilt axis. This effect is similar to ellipticity in diffraction data caused by anisotropic strain, although in our case, decoupling the influences of strain and changes in preferential atomic orientations is not possible. For this reason, we consider changes in the major axis of the fitted ellipse to correspond broadly to changes in the average bond length, *l*, as a function of orientation through the film. l_{xx} is along the *x*-axis, l_{zz} in the *y*–*z* plane along the *z*′-axis, and l_{xx} bisects the *x*′ and *z*′ directions. The stage tilt is limited to 40° in the TitanX, but the OOP bond

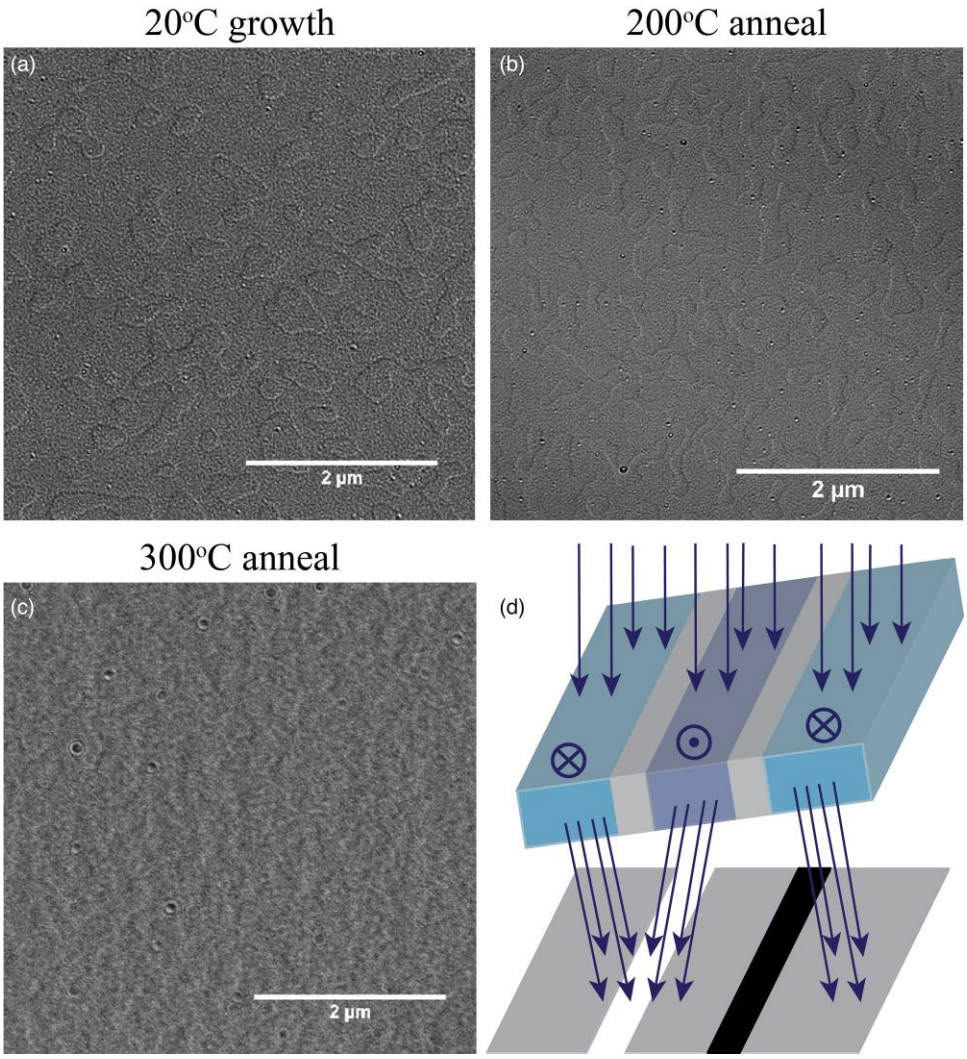

Fig. 4. (**a**–**c**) Lorentz TEM images collected in an FEI ThemIS operated at 300 kV in Lorentz mode from the films (**a**) deposited at 20°C, (**b**) annealed at 200°C that show the typical high-contrast domain patterns seen in films with strong H_c, and (**c**) annealed at 300°C with substantially less pronounced domain structure. The domains are significantly denser and less defined in the film annealed at 300°C compared to the films deposited at 20°C and annealed at 200°C. (**d**) A schematic depiction of the electron beam interacting with a magnetic sample and deflecting to produce contrast in Lorentz TEM. The sample was tilted to 15° and the magnetic field of the objective lens was minimized to <0.1 T, revealing Néel-type domains.

length can be extrapolated from measurements at lower angles by considering the geometry of the experiment and the influence of infinitesimal shifts in bond length on the diffraction data, which gives a $\sin^2$ dependence to the projected OOP bond length. As shown in Figure 3, l_{xx} is modeled with a linear fit and l_{xz} is modeled with a $\sin^2(\theta)/\sqrt{2}$ dependence. The extrapolated value of l_{zz} is obtained by fitting according to the $\sin^2(\theta)$ geometric dependence, as derived and illustrated in Supplementary Figure S4 of the supplementary materials.

Figure 3 shows the trend in average relative % change in mean bond length according to the fitted data (Supplementary Materials) as a function of tilt angle for the films grown at 20 and 300°C. Relative % change below the ±0.2% margin of error indicates that the films are isotropic within the limit of the technique.

From the l_{zz} fits, the extrapolated maximum bond lengths are calculated. For the film deposited at 20°C, the extrapolated maximum relative % change in mean bond length is 1.4%. For the film deposited at 300°C, the extrapolated maximum relative % change in mean bond length is 3.1%. These values are determined by extending the fitting curves to a theoretical 90° tilt, as described in the Supplementary Materials. Both films exhibit shorter mean bond lengths in the IP direction compared to the OOP direction. The IP bond lengths in the film grown at 300°C are larger, on average, than the bonds in the OOP orientation. Assuming the texturing model for PMA, this corresponds to a greater proportion of Co–Tb bonds in the OOP orientation relative to Co–Co bonds in the IP orientations. The greater relative % change in mean bond length for 300°C indicates that at higher deposition temperatures adatoms with higher energies at impingement orient such that Co–Tb bonds form preferentially in the OOP direction, consistent with EXAFS data on *a*-Tb-Fe films (Harris et al., 1992, 1993).

The decrease in H_c and PMA (Ceballos-Sanchez, 2019) between the film grown at 20°C and the films annealed at higher temperatures and the corresponding change in MRO prompted the use of Lorentz TEM. The Lorentz images, shown in Figure 4, corroborate the trends observed in variance, PMA, and coercivity for *a*-$Tb_{17}Co_{83}$ annealed at

increasing temperatures (Hellman et al., 1999; Ceballos-Sanchez, 2019). Coercivity H_c is a measure of the films ability to resist demagnetization in a magnetic field.

Lorentz TEM was applied to the film grown at 20°C and the films grown at 20°C and subsequently annealed at 200 and 300°C to visualize the changes in coercivity. At a tilt angle of 15° in the TEM, the domain structure was substantially more visible than when the beam was perpendicular to the films, indicating that the domain walls are Néel type. Néel walls, typically found in thin films, form when the magnetization rotates within the plane of the film, reducing the demagnetizing energy compared to Bloch walls, which have magnetization rotating out of the plane. The contrast pattern of light and dark denoting the domain walls results from deflection of the electron beam as it interacts with the magnetization of the sample, as shown in Figure 4.

The 20 and 200°C anneal films, which exhibit similar MRO and PMA, show similar domain structures characterized by narrower domain walls, with well-defined domains, as shown in Figures 4a and 4b. However, the 300°C anneal, which exhibits less MRO and lower PMA, has wider and less defined domain walls, as shown in Figure 4c. The result is sharper domain walls and better-defined domains in films deposited at higher temperatures, and less defined domains with wider walls and lower H_c in films grown at lower temperatures after annealing. This observation correlates with the measured coercivities of the *a*-$Tb_{17}Co_{83}$ films and links increased MRO to more defined domain structures due to atomic arrangements resulting in a higher energy cost of domain wall formation. This study demonstrates the influence of annealing and structural order in determining the magnetic domain wall structure and coercivity in the films.

The changes in mean bond length with varying orientation through the films, the increase in MRO as the deposition temperature increases, and the subsequent decrease in MRO after annealing, collectively indicate the presence of MRO bond length anisotropy in the *a*-$Tb_{17}Co_{83}$ films. During deposition, structural variations are introduced as a function of growth temperature. A higher deposition temperature favors a higher proportion of Tb-Co bonds in the OOP direction, which results in greater MRO and increased PMA which leads to increased H_c. Annealing, however, allows for structural relaxation in the films and atom rearrangement which reduces MRO and both PMA and H_c. Taken together, the observed trends in MRO with respect to growth conditions suggest that the evolution of bulk magnetism in the films is due to structural changes. The use of tilted FEM allows or conclusions to be drawn on the relationship between the OOP microstructure and OOP coercivity. A similar approach could be used to probe anisotropic MRO in materials with a range of directionally dependent bulk properties.

Conclusions

Numerous studies on amorphous RE–TM films note the relationships between growth parameters and magnetization, but the structural origin remains under debate. This work established a relationship between thermal growth parameters, magnetic anisotropy and coercivity, and local atomic ordering using the TEM technique of scanning nanodiffraction. MRO increases with increasing film deposition temperature and decreases with increasing anneal temperature. Thus, there is a correlation between the degree of MRO and magnetic anisotropy and coercivity in *a*-$Tb_{17}Co_{83}$ films grown via magnetron co-sputtering. These results support an amorphous phase texturing model in which adatom configuration varies as a function of deposition temperature and annealing allows for subsequent relaxations of preferential configurations within the films. Tilted FEM data shows greater local ordering anisotropy in the film exhibiting the highest degree of MRO compared to the film grown at 20°C with less MRO. The use of FEM with both a tilted and standard sample orientation enable the measurement of relative structural ordering in amorphous materials. This workflow is not limited to amorphous magnetic materials and can be extended to all amorphous thin films displaying anisotropic bulk properties.

Availability of Data and Materials

The data that support the findings of this study are available from the corresponding author, M.S., upon reasonable request. FEM data are openly available in Zenodo at https://doi.org/10.5281/zenodo.8045363. The scripts used to process the FEM data are available at https://github.com/ScottLabUCB/FEM.

Supplementary Material

To view supplementary material for this article, please visit http://academic.oup.com/mam/article-lookup/doi/10.1093/mam/ozae113#supplementary-data.

Acknowledgments

Work at the Molecular Foundry was supported by the Office of Science, Office of Basic Energy Sciences, of the U.S. Department of Energy under Contract No. DE-AC02-05CH11231.

Financial Support

This work was supported by National Science Foundation STROBE grant DMR-1548924. Work at the Molecular Foundry was supported by the Office of Science, Office of Basic Energy Sciences, of the U.S. Department of Energy under Contract No. DE-AC02-05CH11231. Growth and non-electron microscopy characterization of experimental amorphous films were performed by D.O. and E.H. and supported by the U.S. Department of Energy, Office of Science, Basic Energy Sciences, Materials Sciences and Engineering Division under Contract No. DE-AC02-05-CH11231, under the Nonequilibrium Magnetic Materials Program (KC2204). C.O. acknowledges support from the US Department of Energy Early Career Research Program.

Conflict of Interest

The authors declare no conflicts of interest.

References

Andreenko AS & Nikitin SA (1997). Magnetic properties of amorphous rare-earth–3D-transition-metal alloys. *Phys-Uspekhi* **40**(6), 581–597. https://doi.org/10.1070/PU1997v040n06ABEH000245

Bernal JD & Mason J (1960). Packing of spheres: Co-ordination of randomly packed spheres. *Nature* **188**(4754), 910–911. https://doi.org/10.1038/188910a0

Brooks MSS, Eriksson O & Johansson B (1989). 3D-5D band magnetism in rare earth transition metal intermetallics: LuFe2. *J Phys*

Condens Matter **1**(34), 5861–5874. https://doi.org/10.1088/0953-8984/1/34/004

Ceballos A, Pattabi A, El-Ghazaly A, Ruta S, Simon CP, Evans RFL, Ostler T, Chantrell RW, Kennedy E, Scott M, Bokor J & Hellman F (2021). Role of element-specific damping in ultrafast, helicity-independent, all-optical switching dynamics in amorphous (Gd,Tb)Co thin films. *Phys Rev B* **103**(2), 024438. https://doi.org/10.1103/PhysRevB.103.024438

Ceballos-Sanchez A (2019). Characterization and manipulation of temperature-driven magnetic phenomena: Magnetic transition in FeRh thin films and ultrafast magnetization reversal in a-$Gd_{22-x}Tb_xCo_{78}$ thin films. Doctoral dissertation, UC Berkeley. Available at https://escholarship.org/uc/item/76k864xq

Cheng YQ & Ma E (2011). Atomic-level structure and structure–property relationship in metallic glasses. *Prog Mater Sci* **56**(4), 379–473. https://doi.org/10.1016/j.pmatsci.2010.12.002

Cirillo C, Barone C, Bradshaw H, Urban F, Di Bernardo A, Mauro C, Robinson JWA, Pagano S & Attanasio C (2020). Magnetotransport and magnetic properties of amorphous $NdNi_5$ thin films. *Sci Rep* **10**(1), 13693. https://doi.org/10.1038/s41598-020-70646-2

Clark AE (1973). High-field magnetization and coercivity of amorphous rare-earth-Fe_2 alloys. *Appl Phys Lett* **23**(11), 642–644. https://doi.org/10.1063/1.1654777

Cochrane RW, Harris R & Zuckermann MJ (1978). The role of structure in the magnetic properties of amorphous alloys. *Phys Rep* **48**(1), 1–63. https://doi.org/10.1016/0370-1573(78)90012-1

Ding J, Ji D, Yue Y & Smedskjaer MM (2024). Amorphous materials for lithium-ion and post-lithium-ion batteries. *Small* **20**(5), 2304270. https://doi.org/10.1002/smll.202304270

Ding M & Poon SJ (2013). Tunable perpendicular magnetic anisotropy in GdFeCo amorphous films. *J Magn Magn Mater* **339**, 51–55. https://doi.org/10.1016/j.jmmm.2013.03.007

Dirks AG & Gijsbers JRM (1979). Crystallization of amorphous rare earth-iron and transition metal-boron thin films. *Thin Solid Films* **58**(2), 333–337. https://doi.org/10.1016/0040-6090(79)90267-0

Finley J & Liu L (2016). Spin-orbit-torque efficiency in compensated ferrimagnetic cobalt-terbium alloys. *Phys Rev Appl* **6**(5), 054001. https://doi.org/10.1103/PhysRevApplied.6.054001

Fu H & Mansuripur M (1992). Boltzmann distribution of bond orientations and perpendicular anisotropy in amorphous rare-earth–transition-metal films. *Phys Rev B* **45**(13), 7188–7195. https://doi.org/10.1103/PhysRevB.45.7188

Gambino RJ (1998). Amorphous rare earth-transition metal alloys for magneto-optical storage. *MRS Online Proc Libr* **517**, 555–564. https://doi.org/10.1557/PROC-517-555

Ganguly G (2023). Improved sustainability of solar panels by improving stability of amorphous silicon solar cells. *Sci Rep* **13**(1), 10512. https://doi.org/10.1038/s41598-023-37386-5

Greer AL (1995). Metallic glasses. *Science* **267**(5206), 1947–1953. https://doi.org/10.1126/science.267.5206.1947

Hajjar RA, Zhou FL & Mansuripur M (1990). Magneto-optical measurement of anisotropy energy constants on amorphous rare-earth transition-metal alloys. *J Appl Phys* **67**(9), 5328–5330. https://doi.org/10.1063/1.344600

Harris VG, Aylesworth KD, Das BN, Elam WT & Koon NC (1992). Structural origins of magnetic anisotropy in sputtered amorphous Tb-Fe films. *Phys Rev Lett* **69**, 1939–1942. https://doi.org/10.1103/PhysRevLett.69.1939

Harris VG, Elam WT, Koon NC & Hellman F (1994). Deposition-temperature dependence of structural anisotropy in amorphous Tb-Fe films. *Phys Rev B* **49**, 3637–3640. https://doi.org/10.1103/PhysRevB.49.3637

Harris VG, Hellman F, Elam WT & Koon NC (1993). Substrate temperature effect on the structural anisotropy in amorphous Tb-Fe films. *J Appl Phys* **73**, 5785–5787. https://doi.org/10.1063/1.353572

Hasegawa R, Gambino RJ, Cuomo JJ & Ziegler JF (1974). Effect of thermal annealing and ion radiation on the coercivity of amorphous Gd-Co films. *J Appl Phys* **45**, 4036–4040. https://doi.org/10.1063/1.1663908

Hellman F (1994). Surface-induced ordering: A model for vapor-deposition growth of amorphous materials. *Appl Phys Lett* **64**(15), 1947–1949. https://doi.org/10.1063/1.111751

Hellman F & Gyorgy EM (1992). Growth-induced magnetic anisotropy in amorphous Tb-Fe. *Phys Rev Lett* **68**(9), 1391–1394. https://doi.org/10.1103/PhysRevLett.68.1391

Hellman F, Shapiro AL, Abarra EN, Rooney PW & Tran MQ (1999). Magnetic anisotropy and coercivity in magneto-optical recording materials. *J Magn Soc Jpn* **23**(S1), 79–84. https://doi.org/10.3379/jmsjmag.23.S1_79

Hellman F, van Dover RB, Nakahara S & Gyorgy EM (1989). Magnetic and structural investigation of the composition dependence of the local order in amorphous Tb-Fe. *Phys Rev B* **39**(15), 10591–10605. https://doi.org/10.1103/PhysRevB.39.10591

Kennedy E, Reynolds N, Rangel DaCosta L, Hellman F, Ophus C & Scott MC (2020). Tilted fluctuation electron microscopy. *Appl Phys Lett* **117**, 091903. https://doi.org/10.1063/5.0015532

Kiryukhantsev-Korneev PV, Sytchenko AD, Kozlova NS, Zabelina EV, Skryleva EA, Kaplansky YY, Vakhrushev RA & Levashov EA (2022). Structure and properties of protective amorphous ZrBN coating. *Surf Coat Technol* **448**, 128849. https://doi.org/10.1016/j.surfcoat.2022.128849

Kobayashi H, Ono T, Tsushima A & Suzuki T (1983). Large uniaxial magnetic anisotropy in amorphous Tb-Fe evaporated thin films. *Appl Phys Lett* **43**, 389–390. https://doi.org/10.1063/1.94354

Leamy HJ & Dirks AG (1978). Microstructure and magnetism in amorphous rare-earth-transition-metal thin films. I. Microstructure. *J Appl Phys* **49**, 3430–3438. https://doi.org/10.1063/1.325249

Li TT, Bogle SN & Abelson JR (2014). Quantitative fluctuation electron microscopy in the STEM: Methods to identify, avoid, and correct for artifacts. *Microsc Microanal* **20**, 1605–1618. https://doi.org/10.1017/S1431927614012756

Lim S-M, Yeon H-W, Lee G-B, Jin M-G, Lee S-Y, Jo J, Kim M & Joo Y-C (2019). Thermally stable amorphous oxide-based Schottky diodes through oxygen vacancy control at metal/oxide interfaces. *Sci Rep* **9**, 7872. https://doi.org/10.1038/s41598-019-44421-x

Mergel D, Heitmann H & Hansen P (1993). Pseudocrystalline model of the magnetic anisotropy in amorphous rare-earth–transition-metal thin films. *Phys Rev B* **47**, 882–891. https://doi.org/10.1103/PhysRevB.47.882

Nakhmanson SM, Voyles PM, Mousseau N, Barkema GT & Drabold DA (2001). Realistic models of paracrystalline silicon. *Phys Rev B* **63**(23), 235207. https://doi.org/10.1103/PhysRevB.63.235207

Sun Y, Concustell A & Greer AL (2016). Thermomechanical processing of metallic glasses: Extending the range of the glassy state. *Nat Rev Mater* **1**, 1–14. https://doi.org/10.1038/natrevmats.2016.39

Treacy MMJ, Gibson JM, Fan L, Paterson DJ & McNulty I (2005). Fluctuation microscopy: A probe of medium range order. *Rep Prog Phys* **68**(12), 2899–2944. https://doi.org/10.1088/0034-4885/68/12/R06

Vas'kovskiy VO, Adanakova OA, Balymov KG, Kulesh NA, Svalov AV & Stepanova EA (2015). Specific features of the formation of atomic magnetic moments in amorphous films RE-Co (RE = La, Gd, Tb). *Phys Solid State* **57**(6), 1142–1147. https://doi.org/10.1134/S1063783415060335

Voyles PM & Muller DA (2002). Fluctuation microscopy in the STEM. *Ultramicroscopy* **93**(2), 147–159. https://doi.org/10.1016/S0304-3991(02)00155-9

Williamson DL (1995). Nanostructure of a-Si:H and related materials by small-angle x-ray scattering. *MRS Online Proc Libr* **377**, 251–262. https://doi.org/10.1557/PROC-377-251

Xue L, Shao L, Han Z, Luo Q, Wang H, Huo J, Li Z, Zhang B, Cheng J & Shen B (2022). Tunable magnetocaloric effect in Gd-based metallic glasses microalloying elements with different magnetism. *J Non Cryst Solids* **576**, 121222. https://doi.org/10.1016/j.jnoncrysol.2021.121222

Yan X, Hirscher M, Egami T & Marinero EE (1991). Direct observation of anelastic bond-orientational anisotropy in amorphous $Tb_{26}Fe_{62}Co_{12}$ thin films by x-ray diffraction. *Phys Rev B* **43**(11), 9300–9303. https://doi.org/10.1103/PhysRevB.43.9300

Yu Y, Zhang Q, Xu Z, Zheng W, Xu J, Xi Z, Zhu L, Ding C, Cao Y, Zheng C, Qin Y, Li S, Li A, Wu D, Rabe KM, Liu X & Wen Z (2023). Structure-evolution-designed amorphous oxides for dielectric energy storage. *Nat Commun* **14**(1), 3031. https://doi.org/10.1038/s41467-023-38847-1

Zhang WY, Shima H, Takano F, Takenaka M, Yamazaki M, Masuda K, Akinaga H, Nagahama T & Nimori S (2010). Origin of perpendicular magnetic anisotropy and evolution of magnetic domain structure of amorphous Pr–TM–B (TM=Fe, Co) films. *J Magn Magn Mater* **322**(8), 900–908. https://doi.org/10.1016/j.jmmm.2009.11.022

Zhu Y, Kennedy ER, Yasar B, Paik H, Zhang Y, Hood ZD, Scott M & Rupp JL (2024). Uncovering the network modifier for highly disordered amorphous Li-garnet glass-ceramics. *Adv Mater* **36**(16), e2302438. https://doi.org/10.1002/adma.202302438